Dynamic Stall Development

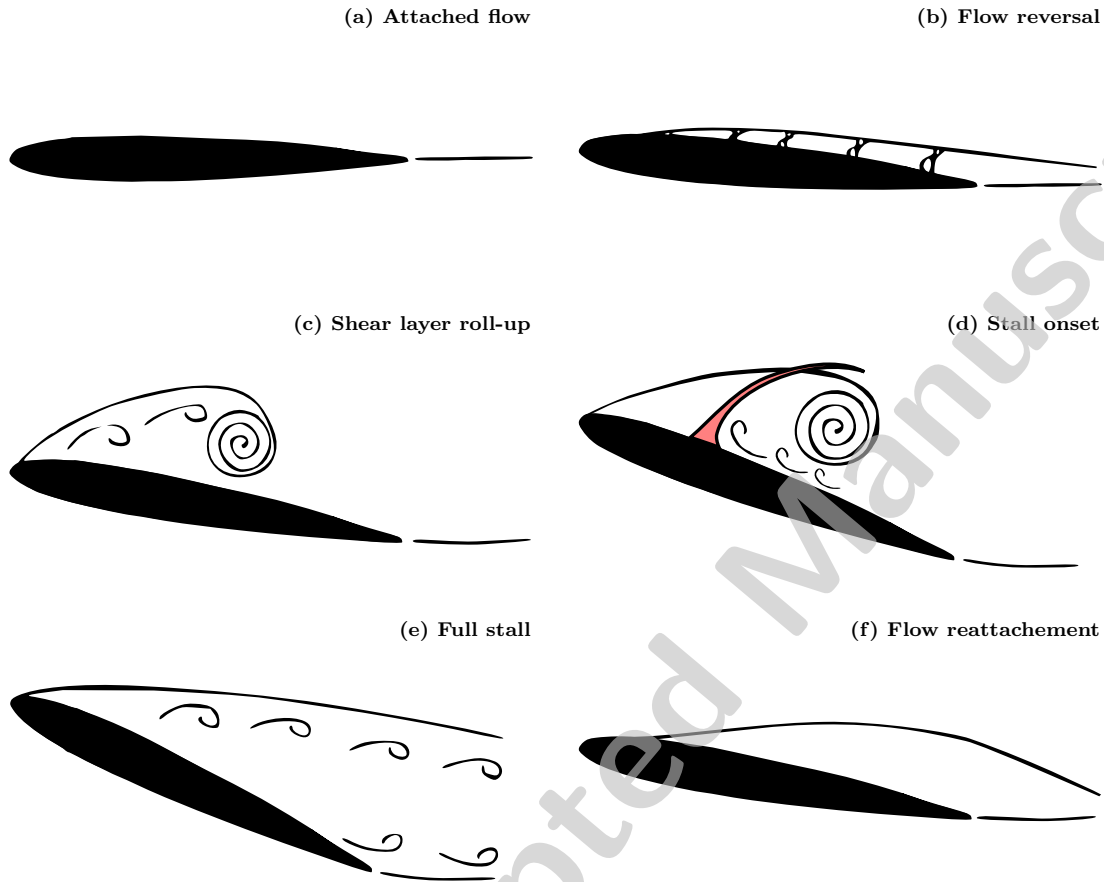**Karen Mulleners · Markus Raffel**

Abstract Dynamic stall on an oscillating airfoil was investigated by a combination of surface pressure measurements and time-resolved particle image velocimetry. Following up on previous work on the onset of dynamic stall (Mulleners and Raffel 2012), we combined time-resolved imaging with extensive coherent structure analysis to study various aspects of stall development. The formation of the primary dynamic stall vortex was identified as the growth of a recirculation region and the ensuing instability of the associated shear layer. The stall development can be subdivided into two stages of primary and secondary instability with the latter being the effective vortex formation stage. The characteristic time scales associated with the primary instability stage revealed an overall decrease of dynamic stall delay with increasing effective unsteadiness of the pitching airfoil. The vortex formation stage was found to be largely unaffected by variations of the airfoil's dynamics.

List of Symbols

c	chord length
C_l	lift coefficient
C_p	pressure coefficient
$C_{p,min}$	minimum surface pressure level
f_{osc}	pitching frequency
k	reduced frequency
Ma	Mach number
N	number of clockwise rotating vortices
Re	Reynolds number
t_{ss}	passage of the static stall angle during upstroke
t^*	onset of shear layer roll-up
t_{ds}	dynamic stall onset
T	oscillation period
$\mathbf{u} = (u, v, w)$	local velocity
U_∞	free steam velocity
$\mathbf{x} = (x, y, z)$	spatial coordinates
$\mathbf{x}_{vi} = (x_{vi}, 0, z_{vi})$	position of the vortex v_i
$\mathbf{x}_w = (x_w, y_w, z_w)$	airfoil coordinates
α	angle of attack
α_0	mean incidence
α_1	oscillation amplitude
α^*	angle of attack at the onset of shear layer roll-up
α_{ds}	dynamic stall angle of attack
α_{ss}	static stall angle of attack
$\dot{\alpha}_{ss}$	instantaneous effective unsteadiness
Γ	scalar function
ν	kinematic viscosity
Δt_1	stall delay attributed to the *primary instability stage*
Δt_2	stall delay attributed to the *vortex formation stage*
Δz	average shear layer displacement
ω	vorticity
$\nearrow$	during upstroke
$\searrow$	during downstroke

K. Mulleners ( ) · M. Raffel
German Aerospace Center (DLR),
Bunsenstr. 10, 37073 Göttingen, Germany
Present address: of K. Mulleners
Institute of Turbomachinery and Fluid Dynamics,
Leibniz Universität Hannover, Germany
E-mail: mulleners@tfd.uni-hannover.de

(a) Attached flow

(b) Flow reversal

(c) Shear layer roll-up

(d) Stall onset

(e) Full stall

(f) Flow reattachement

Fig. 1 Schematic representation of the different stages of the dynamic stall process (modified from Doligalski and Smith (1994) and Carr et al (1977)).

1 Introduction

Dynamic stall (DS) occurs on helicopter or wind turbine rotor blades in response to an unsteady change of the angle of attack beyond the static stall angle. It is characterised by the formation of a large-scale dynamic stall vortex and a delayed onset of massive flow separation with respect to static stall (McAlister et al 1978; McCroskey 1981; Carr 1988).

Highly unsteady aerodynamic loads during dynamic stall decrease the aerodynamic efficiency while increasing structural forces and bending moments. Since DS is the key to agility, manoeuvrability, and structural stability of rotary wings, improving dynamic stall modelling and prediction capabilities is highly desirable. For this purpose accurate knowledge of the unsteady flow field and associated vortex dynamics during dynamic stall development is essential.

Based on a combination of time-resolved velocity field information and extensive coherent structure analysis, the development of the unsteady flow over an os-

cillating airfoil within a single dynamic stall life cycle was previously classified into five successive stages: the *attached flow stage*; the *stall development stage*; *stall onset*; the *stalled stage*; and *flow reattachment* (Mulleners and Raffel 2012). Due to the unsteady nature of the process, time-resolved measurement methods are required to analyse the chronology and causality of the prominent stall events (figure 1) (Carr et al 1977; Shih et al 1992).

The stall development stage is the part of the DS life cycle between static and dynamic stall onset covering the unsteady separation process. The flow separation is initiated by an adverse pressure gradient and involves the formation and detachment of a shear layer from the airfoil's surface (Reynolds and Carr 1985; Degani et al 1998). With increasing angle of attack beyond static stall, an adverse pressure gradient builds up and leads to the formation of a prominent recirculation region that grows normal to the surface (figure 1(b)). At the interface between regions of reverse and free stream flow, a shear layer develops that controls the succes-

sive stall development (Ho 1986). The primary insta-
bility of the shear layer generates small-scale vortices
that interact only weakly at first. Subsequently, vis-
cous interactions increase leading to the roll-up of the
shear layer into a large-scale DS vortex (figure 1(c)).
The primary stall vortex subsequently detaches due to
vortex induced separation signalising dynamic stall on-
set (figure 1(d)) (Obabko and Cassel 2002). The onset
of dynamic stall can be readily specified directly from
the velocity field based on a characteristic mode of the
proper orthogonal decomposition (POD) of the velocity
field (Mulleners and Raffel 2012).

Following up on that work, this paper focusses on
the identification and characterisation of the physical
mechanisms and parameters controlling initiation, growth,
and subsequent detachment of the DS vortex. In order
to sustain and further improve dynamic stall modelling,
special emphasis is placed on the role and behaviour of
the shear layer and the associated time scales. A combi-
nation of time-resolved velocity field information with
different coherent structure detection methods serves to
fulfil the above objectives.

2 Materials and Methods

Unsteady surface pressure and time-resolved particle
image velocity (TR-PIV) measurements were conducted
in the central cross sectional plane of a pitching OA209
airfoil (figure 2). The velocity field was measured with
a spatial resolution of 1.2 mm at an acquisition rate
of 1500 Hz (6 kHz for the pressure distribution). The
two-dimensional airfoil model with an OA209 profile of
chord length $c = 0.3$ m was placed in a uniform flow at
free stream Reynolds number $Re = \dfrac{U_\infty c}{\nu} = 9.2 \times 10^5$
with U_∞ the free stream velocity and ν the kinematic
viscosity (Mach number $Ma = 0.14$). The airfoil was
subjected to a sinusoidal oscillation about its quarter
chord axis with mean incidence α_0, amplitude α_1, and
reduced frequency k. The latter is defined as $k = \pi f_{osc} c/U_\infty$
with f_{osc} the pitching frequency. Mean incidence, am-
plitude and reduced frequency were varied to attain dif-
ferent stall cases.

The time-resolved PIV data was evaluated accord-
ing to standard procedures (Raffel et al 2007) using the
multi grid algorithm with image deformation and a final
interrogation window size of 32 px × 32 px and an over-
lap of approximately 80 %. This yields a grid spacing
or physical resolution of 6 px or 1.2 mm = 0.004 c.

The detection probability of a valid displacement
in the PIV data was higher than 90%. The remaining
spurious vectors were detected and replaced using the
automated post-processing algorithm of Garcia (2010).
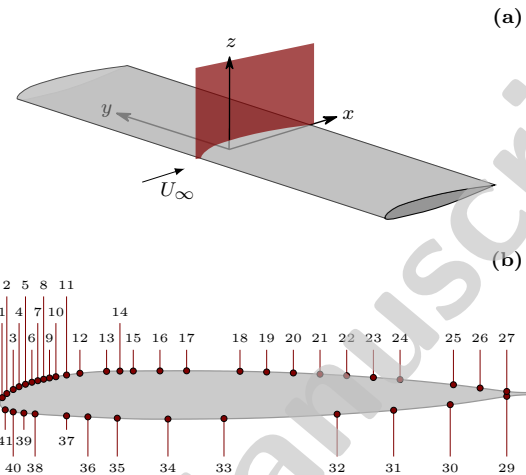
Fig. 2 Position of the PIV field of view (a) and location of the
unsteady pressure sensors in the mid-span section of the OA209
airfoil profile (b).

The inaccuracy in determining the valid displacements
is given by the single displacement error ϵ_x, which is
decomposed into the random error or measurement un-
certainty ϵ_{rms} and the bias error ϵ_{bias}. The random er-
ror refers to measurement uncertainties induced and af-
fected by the particle image diameter, the size of the in-
terrogation window size, and the particular flow condi-
tions. The interrogation windows size has an important
influence on the measurement uncertainty which in-
creases with decreasing interrogation window size Raffel
et al (2007). For a good compromise between a high
spatial resolution and a low random error, the data
was evaluated with a final window size of 32 px × 32 px.
Based on careful analysis of the results, the random er-
ror was estimated smaller than 0.05 px for observation
areas containing uniform flow and 0.1 px for observation
areas where strong velocity gradients are present. The
bias error is mainly determined by peak-locking, a phe-
nomenon describing the tendency of the displacements
to be biased towards integer pixel values. Histograms
of subpixel displacement showed that peak locking was
successfully avoided and the remaining bias error was
assumed to be significantly less than the random noise
error, i.e. $\epsilon_{bias} < 0.05$ px.

The total error for the velocity measurement is now
determined by dividing the single displacement error
by the pulse-separation time Δt and the magnifica-
tion factor of the camera recording M according to
$\epsilon_{vel} = \dfrac{\epsilon_x}{\Delta t\, M}$. The measurement error is often made
dimensionless by the mean free flow velocity yielding a
relative error $\epsilon_{rel} = \epsilon_{v,in}/U_\infty \leq 0.02$. Due to the record-
ing geometry and random character of the measurement
uncertainty, the measurement error for the out-of-plane

velocity component was estimated to be a factor of 2 higher than for the in-plane components.

Prior to analysis, the velocity fields were rotated into the airfoil reference system with the x-axis along the chord, the y-axis along the span and the z-axis upward perpendicular to the chord, while the origin coincides with the rotation axis, i. e. the airfoil's quarter chord axis, at model mid-span.

The characteristic flow features were identified and analysed using an Eulerian and a Lagrangian procedure. The Eulerian method utilises the dimensionless scalar function Γ introduced by Michard et al (1997) to locate the axis of individual vortices and to determine their sense of rotation. The Lagrangian approach adopted was the finite-time Lyapunov exponent (FTLE) method (Haller and Yuan 2000). Particle trajectories were integrated forward and backward in time, yielding positive and negative finite-time Lyapunov exponent fields (pFTLE and nFTLE fields). The ridges in the FTLE fields indicate the boundaries of Lagrangian coherent structures (LCS) (Shadden et al 2005). The FTLE fields were calculated based on the in-plane velocity field with the software package *ManGen* created by Lekien and Coulliette (Lekien et al 2005).

3 Results and Discussion

Following up on the specification of the dynamic stall onset (Mulleners and Raffel 2012), we focus here on the identification and characterisation of the individual physical mechanisms and relevant time scales of the flow development prior to stall onset. To repeat the overall flow development during a single dynamic stall life cycle, instantaneous velocity fields and surface pressure distributions for the harmonic oscillation specified by $\alpha_0 = 20°$, $\alpha_1 = 8°$ and $k = 0.10$ are depicted in figure 3 for the different stages of the dynamic stall process summarised in figure 1. The presence and location of clockwise and counterclockwise rotating vortices, as determined by the Eulerian detection algorithm, help to identify the characteristic features of the dynamic stall life cycle.

The first noticeable event that occurs during the upstroke motion is the development of a shear layer at the interface between recirculating flow near the upper rear surface of the airfoil and the free stream flow. The shear layer contains only positive vorticity which is clumped into individual shear layer vortices (figure 3(b)). With increasing angle of attack, the region of flow reversal grows. This is accompanied by an increase in the pressure coefficient at the surface underneath the recirculating flow. The leading edge suction peak continues to grow with increasing angle of attack until the shear
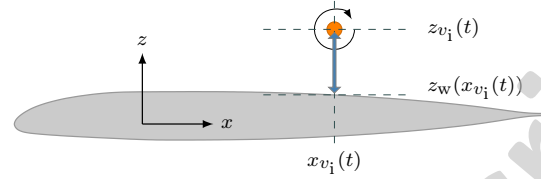

Fig. 4 Schematic representation of the computation of Δz.

layer roll ups into a large scale DS vortex (figure 3(c)). For a short period of time, the DS vortex grows in size while remaining in place until it has grown strong enough to separate as a result of a vortex induced separation process (figure 3(d)). The presence of the large-scale structure can be recognised by a plateau in the surface pressure distribution between approximately $x/c = -0.1$ and $x/c = 0.2$ on the suction side. This scenario of vortex development, where the shear layer rolls up into a large scale coherent structure which grows locally and temporally until separating is generally referred to as wake mode (Gharib and Roshko 1987; Hudy et al 2007). It differs from the shear layer mode where the shear layer continuously rolls up into large scale structures that grow spatially, i.e. while travelling downstream.

The detachment of the DS vortex marks stall onset and the beginning of the stalled stage which is characterised by massive flow separation (figure 3(e)). The stalled stage lasts for most of the rest of the cycle until, near the end of the downstroke, the flow reattaches from the leading edge towards the trailing edge (figure 3(f)).

3.1 Shear Layer Displacement

The prominent feature that plays an important role prior to stall onset is the shear layer. The shear layer limits the recirculation region and it is identified by the small scale shear layer vortices. To quantify and analyse the growth of the recirculation region a new quantity Δz is introduced to represent the average chord-normal distance of the shear layer from the airfoil's upper surface. Considering the shear layer as a vortex sheet containing individual small-scale vortices resulting from the primary instability, Δz is calculated as the average chord-normal height of all clockwise rotating vortical structures in individual experimental snapshots of the velocity field or

$$\Delta z(t) = \frac{1}{N(t)} \sum_{i=1}^{N(t)} \left| z_{v_i}(t) - z_w(x_{v_i}(t)) \right| \quad . \tag{1}$$

Here, $N(t)$ is the total number of clockwise rotating vortices at time t according to the Eulerian vortex detection algorithm and $\left| z_{v_i}(t) - z_w(x_{v_i}(t)) \right|$ is the chord-
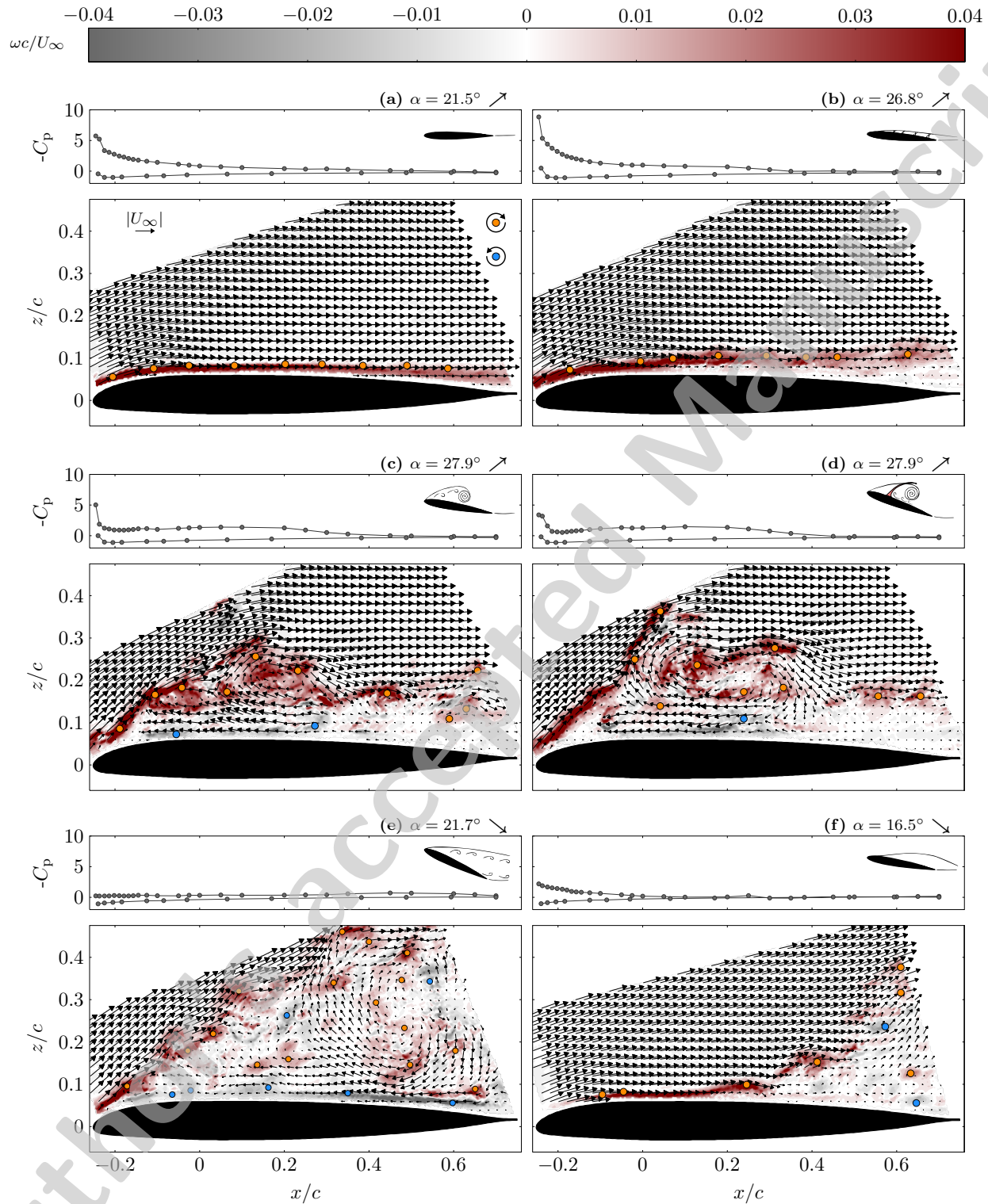
Fig. 3 Instantaneous flow fields with detected vortex cores: (•) clockwise and (•) anticlockwise rotation; and the respective surface pressure distribution for the different stall development stages within a single oscillation ($\alpha_0 = 20°$, $\alpha_1 = 8°$, and $k = 0.10$). Only every sixth velocity vector is shown for the sake of visibility and the dimensionless out–of–plane component of the vorticity is colour–coded.
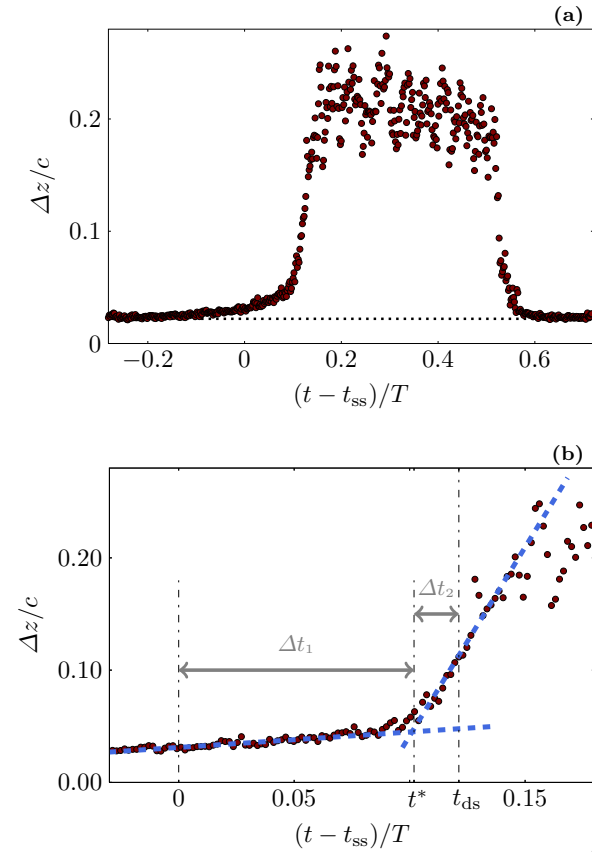
Fig. 5 Temporal evolution of the average shear layer height in terms of Δz over one oscillation period T (a), with a detailed view (b) including the corresponding linear fits to the data. The dotted line in (a) indicates the noise level due to experimental limitations. The time axis is shifted with respect to the passage of the static stall angle during upstroke t_{ss}. The onset of dynamic stall is indicated by t_{ds} ($\alpha_0 = 20°$, $\alpha_1 = 8°$, $k = 0.05$).

normal distance of the individual vortices v_i to the airfoil's upper surface as illustrated in figure 4.

A representative temporal evolution of Δz for one oscillation period T, which starts at minimum incidence, is depicted in figure 5 for $\alpha_0 = 20°$, $\alpha_1 = 8°$, and $k = 0.05$. For small angles of attack, vorticity is *a priori* confined to the thin boundary layer and is convected downstream along the airfoil's contour. The convection dominated vorticity transport limits the boundary layer growth. For a fully attached flow Δz is expected to be constant and of the order of the boundary layer thickness. Due to experimental limitations valid velocity information was only available down to approximately 2 mm above the airfoil's surface. With increasing angle of attack, Δz increases until the flow is massively separated. Near the end of the cycle, Δz decreases to its initial unstalled value, indicating reattachment of the flow.

3.2 Two-stage Stall Development

The most interesting behaviour of Δz is observed during the stall development stage (figure 5). The stall development stage was defined earlier as the part of the DS life cycle where the angle of attack is between the static and dynamic stall onset angle. The static stall onset angle is determined from the static airload data as $a_{ss} = 21.4°$. The time at which the static stall angle is exceeded in the DS cycle is denoted by t_{ss}. The dynamic stall onset angle is specified directly from the measured velocity field based on a characteristic mode of the proper orthogonal decomposition (POD). More specifically, it is determined as the angle of attack for which the time development coefficient of the POD mode representing the large scale DS vortex reaches an extremum. This corresponds directly to the separation of the DS vortex (Mulleners and Raffel 2012). Dynamic stall onset is indicated by a_{ds} and t_{ds}, respectively referring to the angle of attack and the time instant.

The evolution of Δz during the stall development stage exhibits a two-stage linear increase with a distinctly different growth rate. The explanation for the difference and the sudden change in growth rate is provided based on close examination of the flow topology and vortex distribution during the two sub-stages (figure 6).

During the first part of stall development, which is characterised by the slow linear increase of Δz, the recirculation region grows steadily in chord-normal direction. Small-scale co-rotating vortices emerge in the shear layer due to a primary instability. These shear layer vortices are regularly spaced and all rotating clockwisely. They are convected downstream by the external flow and do not merge or overtake each other during this first sub-stage (figure 6(a)). By reference to standard mixing layer notations (Corcos and Sherman 1984), the initial part of stall development is referred to as the *primary instability stage*.

During the later part of stall development, which is characterised by a stronger, but still linear, increase of Δz, the viscous interactions between the small shear layer vortices increase. They merge as a result of a secondary instability leading to shear layer roll-up and the formation of the primary DS vortex. Therefore, this part of stall development is referred to as the *vortex formation stage*.

While the chord-normal distance of the shear layer smoothly increases during the *primary instability stage* due to the growth of the recirculation region, Δz mainly increases due to chord-normal excursions and coalescence of the shear layer vortices during the *vortex formation stage*. When vortex pairs coalesce, the strength
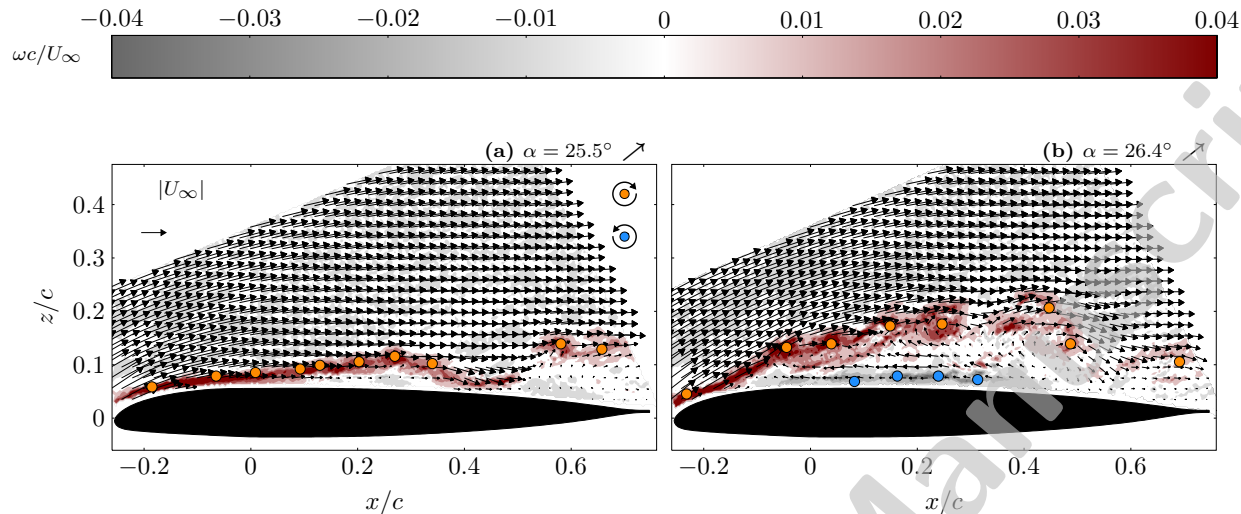
Fig. 6 Difference in flow topology and vortex distribution (clockwise (•) and counter-clockwise (•) rotating vortices) between the *primary instability* (a) and the *vortex formation stage* (b) ($\alpha_0 = 20°$, $\alpha_1 = 8°$, $k = 0.050$).

of the individual vortices and the spacing between them grows binomially doubling the time lag between subsequent coalescences. The growth of a free shear layer is therefore, on average, linear in time (Corcos and Sherman 1984) and the same is true for the increase of the mean height Δz during the *vortex formation stage* (figure 5). The rate of increase of Δz during this stage thus provides a measure for the rate of growth of the dynamic stall vortex.

In addition, the increased circulation around merged vortex pairs enforces stronger interactions between the viscous shear layer and the reversed flow generating counter-rotating vortices near the airfoil's surface (figure 6(b)). These anti-clockwise rotating vortices trigger the onset of dynamic stall as they move towards the leading edge and promote vortex induced separation with increased angle of attack (Mulleners and Raffel 2012).
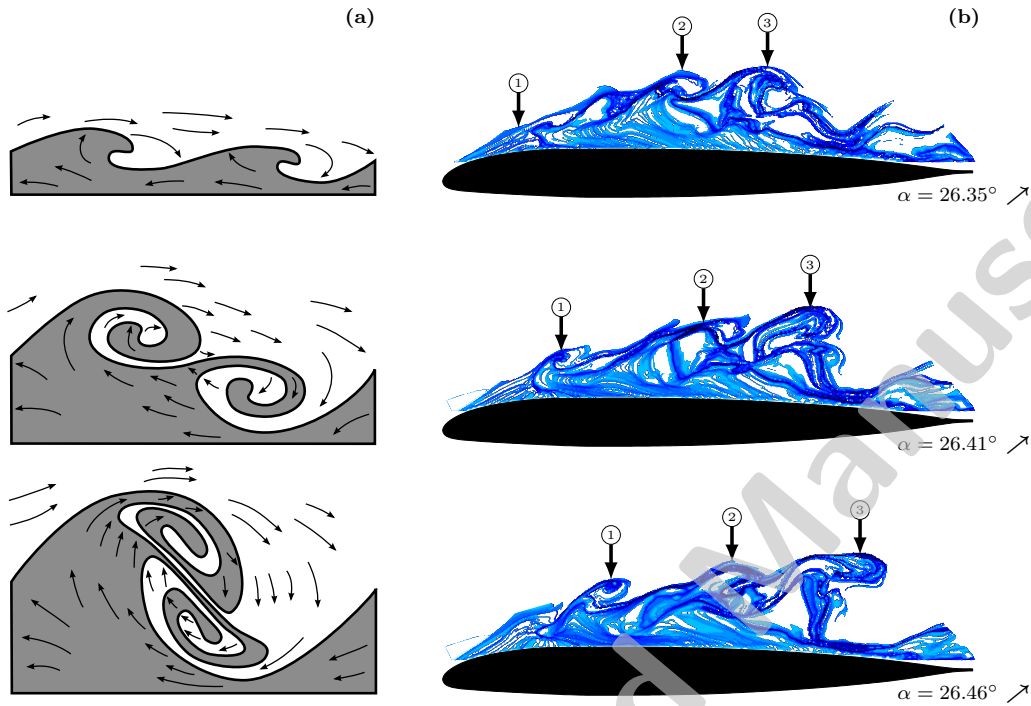
3.3 Transition of the Shear Layer Instability

Based on the change in growth rate of the shear layer height and the different associated shear layer characteristics, stall development is subdivided here into the *primary instability* and the *vortex formation stage*. The transition between both regimes of stall development is specified in the Eulerian framework by the intersection of the two linear fitting curves that approximate the two-stage constant growth of Δz in the individual regimes (figure 5(b)). The time instant and angle of attack at which the transition takes place is denoted by t^* and α^*, respectively.

A sequence of instantaneous negative FTLE fields around $t = t^*$ shows the evolution of the shear layer during transition from the *primary instability stage*, which is governed by inertial effects, and the *vortex formation stage*, which is governed by viscous effects. The ridges in the FTLE field represent material lines that segregate the inviscid free stream flow from the viscous flow within the shear layer. Bulging of the material lines indicate the engulfing process that characterises a secondary instability of the shear layer leading to shear layer roll-up. This process is comparable to the engulfing process during mixing layer roll-up described by Corcos and Sherman (1984) (figure 7(a)).

The transition of the shear layer instability from a primary instability, generating small scale shear layer vortices, to a secondary instability, causing shear layer roll-up, induces an increase in the displacement rate of the shear layer and affects the aerodynamic performance of the airfoil. During the *primary instability stage*, the lift coefficient C_l continuously increases and the first drop of C_l coincides with the transition into the *vortex formation stage*. The lift overshoot with regard to static stall – which is the only desirable attribute of dynamic stall – is thus entirely generated during the *primary instability stage*.

The fundamental difference in shear layer behaviour has a direct impact on the lift coefficient. To improve current semi-empirical engineering models for the prediction of dynamic stall airloads, this is an important observation. In order to replace the empirical parameters in these models by physical relationships, comprehensive knowledge of the governing parameters and

(a) (b)

Fig. 7 Schematic representation of the engulfing process during mixing layer roll-up by Corcos and Sherman (1984) (a) and the development of a secondary instability of the shear layer visualised be the negative FTLE fields, extracted based on instantaneous velocity fields within a single oscillation ($\alpha_0 = 20°$, $\alpha_1 = 8°$, and $k = 0.05$), at consecutive time steps during transition from the *primary instability* into the *vortex formation stage* (b).

their effect on the stall delays attributed to the two substages of stall development is essential.

3.4 Time Scales of Stall Development

Stall delay refers to the time delay between static and dynamic stall onset. According to the splitting of the stall development stage, the overall stall delay is the sum of the time delays attributed to the *primary instability* and *vortex formation stage* denoted by Δt_1 and Δt_2, respectively (figure 5(b)). The separate contributions are specified as $\Delta t_1 = t^* - t_{ss}$ and $\Delta t_2 = t_{ds} - t^*$.

In order to be able to predict the stall delay for arbitrary dynamic stall oscillations in the furture, we need to determine in what pathway the airfoil dynamics affect the time delay contribution of both substages. For a sinusoidal oscillation, the airfoil's motion is described by the interrelated parameters mean incidence, amplitude, and oscillation frequency. These parameters can be combined into a single representative parameter, the instantaneous effective unsteadiness $\dot{\alpha}_{ss}$. The instantaneous effective unsteadiness is defined as the rate of change of the angle of attack when the static stall angle is exceeded. It successfully describes the influence of the unsteadiness of the pitching motion with respect to

the dynamic stall process (Mulleners and Raffel 2012). In particular, a hastened onset of dynamic stall was observed previously with increasing effective unsteadiness.

Considering now the individual stall delays Δt_1 and Δt_2 as a function of the normalised effective unsteadiness $\dot{\alpha}_{ss} c/U_\infty$, additional information is obtained (figure 9(a)). Firstly, the delay due to the *primary insta-*
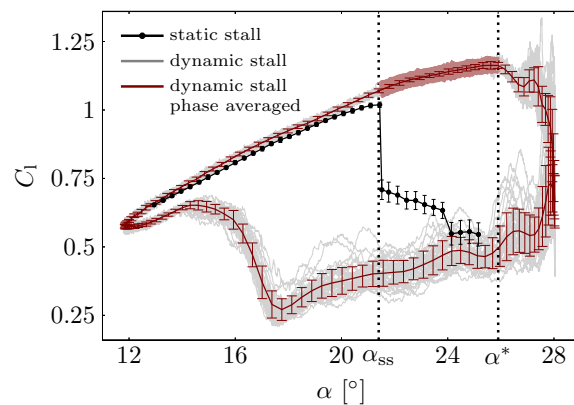
Fig. 8 Lift coefficient as a function of angle of attack for static and dynamic stall. The coloured segment corresponds to the *primary instability stage* ($\alpha_0 = 20°$, $\alpha_1 = 8°$, $k = 0.05$).
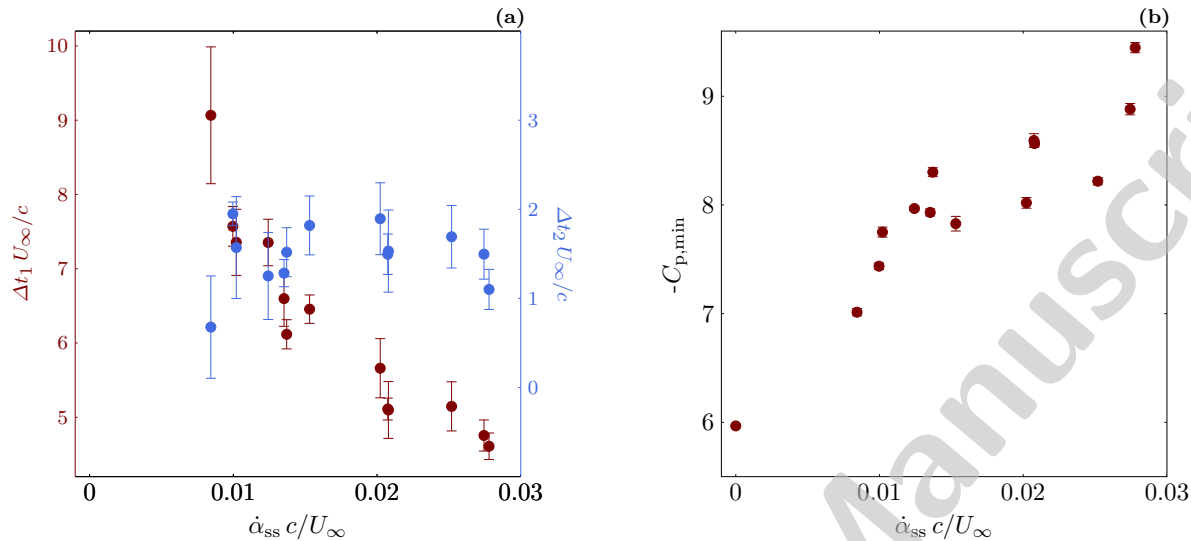
Fig. 9 Influence of the instantaneous effective unsteadiness on the dynamic stall delays Δt_1 and Δt_2 attributed to the *primary instability stage* and the *vortex formation stage*, respectively (a); the minimum surface pressure level $C_{\text{p,min}}$ (b). Error bars indicate the standard deviations.

bility stage is at least double the delay time due to the *vortex formation stage*. Secondly, Δt_2 is approximately constant for all pitching motions considered here. There is no significant influence of the airfoil's motion on the vortex formation process because the shear layer roll-up is mainly governed by viscous interactions between the shear layer vortices. Finally, Δt_1 clearly decreases with increasing effective unsteadiness. When the pitch rate increases, a larger amount of vorticity is generated and accumulates in the shear layer (Acharya and Metwally 1992). The more vorticity accumulates in the shear layer, the faster a secondary shear layer instability sets in, hence the shorter the *primary instability stage* which ends with the transition of the shear layer at t^*. Evidence that vorticity in the shear layer increases with increasing effective unsteadiness is provided in figure 9(b) because increased vorticity in the shear layer leads to a stronger acceleration of the flow or an increased suction peak at the leading edge (Lorber and Carta 1988; Visbal and Shang 1989). As a consequence, the minimum suction peak at dynamic stall must always be larger than at static stall, which is true for the present experiments. In figure 9(b), the static reference case fits well within the trend revealed by the dynamic test conditions.

4 Conclusion and Future Work

The dynamic stall development on a pitching airfoil was discussed based on a combination of time-resolved velocity field information and coherent structure analysis.

Stall development describes the period of time prior to stall onset and covers the emergence and subsequent development of a shear layer at the interface between recirculating and free stream flow. The shear layer is the prominent feature during stall development. Based on different shear layer behaviour, the stall development stage was subdivided into a *primary instability stage* followed by a *vortex formation stage*. The *primary instability stage* essentially covers the growth of the recirculation region and the corresponding initial development and primary instability of the shear layer. The transition from a primary into a secondary shear layer instability leads to a sudden increase in the rate of displacement of the shear layer and the first drop of the lift coefficient. The transition of shear layer instability marks the beginning of the second part of stall development or *vortex formation stage*. The *vortex formation stage* is characterised by the roll-up of the shear layer into the large-scale DS vortex which grows locally and temporally until separating as a result of vortex induced separation. The scenario was identified as wake mode.

The overall stall delay is the sum of the time delays attributed to the *primary instability* and *vortex formation stage*, where the former is at least double as long as the latter. The delay attributed to the *primary instability stage* decreases with increasing unsteadiness and is correlated with the minimum surface pressure level. The larger the instantaneous effective unsteadiness, the more vorticity accumulates in the shear layer, leading to increased suction peaks and promotion of the onset of shear layer roll-up. The relatively small delay

attributed to the *vortex formation stage* is governed by viscous flow interactions and virtually unaffected by variations in the airfoil's pitching motion.

The combination of multiple vortex identification procedures that are different in nature provides a more detailed and more comprehensive insight into unsteady vortex flows than conventional methods are capable of. Future work will focus on: the dynamics of static stall development, three-dimensional aspects of dynamic stall as well as dynamic stall in rotating environments.

References

Acharya M, Metwally MH (1992) Unsteady Pressure Field and Vorticity Production over a Pitching Airfoil. AIAA Journal 30(2):403–411

Carr L, McAlister K, McCroskey W (1977) Analysis of the Development of Dynamic Stall Based on Oscillating Airfoil Experiments. Tech. rep., NASA

Carr LW (1988) Progress in Analysis and Prediction of Dynamic Stall. Journal of Aircraft 25(1):6–17

Corcos G, Sherman F (1984) The mixing layer: deterministic models of a turbulent flow. Part 1. Introduction and the two-dimensional flow. Journal of Fluid Mechanics 139:29–65, DOI 10.1017/S0022112084000252, URL http://www.journals.cambridge.org/abstract_S0022112084000252

Degani A, Walker J, Smith F (1998) Unsteady separation past moving surfaces. Journal of Fluid Mechanics 375:1–38

Doligalski T, Smith C (1994) Vortex interactions with walls. Annual review of fluid 26:573–616, URL http://www.annualreviews.org/doi/pdf/10.1146/annurev.fl.26.010194.003041

Garcia D (2010) A fast all-in-one method for automated post-processing of PIV data. Experiments in Fluids 50(5):1247–1259, DOI 10.1007/s00348-010-0985-y, URL http://www.springerlink.com/index/10.1007/s00348-010-0985-y

Gharib M, Roshko A (1987) The effect of flow oscillations on cavity drag. Journal of Fluid Mechanics 177:501—-530

Haller G, Yuan G (2000) Lagrangian coherent structures and mixing in two-dimensional turbulence. Physica D: Nonlinear Phenomena 147(3-4):352–370, DOI 10.1016/S0167-2789(00)00142-1, URL http://linkinghub.elsevier.com/retrieve/pii/S0167278900001421

Ho CM (1986) An alternative look at the unsteady separation phenomenon. In: Recent advances in aerodynamics, Springer, chap An alterna, pp 165–178

Hudy LM, Naguib A, Humphreys WM (2007) Stochastic estimation of a separated-flow field using wall-pressure-array measurements. Physics of Fluids 19(2):024,103–1—-18, DOI 10.1063/1.2472507, URL http://link.aip.org/link/PHFLE6/v19/i2/p024103/s1&Agg=doi

Lekien FF, Coulliette C, Mariano A, Ryan E, Shay L, Haller G, Marsden J (2005) Pollution release tied to invariant manifolds: A case study for the coast of Floridalease tied to invariant manifolds: A case study for the coast of Florida. Physica D: Nonlinear Phenomena 210:1–20

Lorber P, Carta F (1988) Airfoil Dynamic Stall at Constant Pitch Rate and High Reynolds Number. Journal of Aircraft 25(6):548–556

McAlister K, Carr L, McCroskey W (1978) Dynamic Stall Experiments on the NACA 0012 Airfoil. Tech. rep., NASA

McCroskey WJ (1981) The Phenomenon of Dynamic Stall. Tech. rep., NASA

Michard M, Graftieaux L, Lollini L, Grosjean N (1997) Identification of Vortical Structures by a non Local Criterion - Application to PIV Measurements and DNS-LES Results of Turbulent Rotating Flows. In: Proceedings of the 11th Conference on Turbulent Shear Flows

Mulleners K, Raffel M (2012) The onset of dynamic stall revisited. Experiments in Fluids 52(3):779–793, DOI 10.1007/s00348-011-1118-y, URL http://www.springerlink.com/index/10.1007/s00348-011-1118-y

Obabko aV, Cassel KW (2002) Detachment of the dynamic-stall vortex above a moving surface. AIAA Journal 40(9):1811–1822, DOI 10.2514/3.15264, URL http://arc.aiaa.org/doi/abs/10.2514/3.15264

Raffel M, Willert CE, Wereley ST, Kompenhans J (2007) Particle Image Velocimetry: A Practical Guide. Experimental Fluid Mechanics Series, Springer, URL http://books.google.de/books?id=WH5w2TvK2bQC

Reynolds W, Carr L (1985) Review of Unsteady, Driven, Separated Flows. Tech. rep., AIAA

Shadden SC, Lekien F, Marsden JE (2005) Definition and properties of Lagrangian coherent structures from finite-time Lyapunov exponents in two-dimensional aperiodic flows. Physica D: Nonlinear Phenomena 212(3-4):271–304, DOI 10.1016/j.physd.2005.10.007, URL http://linkinghub.elsevier.com/retrieve/pii/S0167278905004446

Shih C, Lourenco L, Van Dommelen L, Krothapalli A (1992) Unsteady Flow Past an Airfoil Pitching at a Constant Rate. AIAA Journal 30(5):1153–1161

Visbal MR, Shang JS (1989) Investigation of the Flow Structure Around a Rapidly Pitching Airfoil. AIAA Journal 27(8):1044–1051